



1 **The Indonesian Throughflow Circulation Under Solar Geoengineering**

2 Chencheng Shen¹ John C. Moore^{1,2,3*} Heri Kuswanto^{4,5} Liyun Zhao^{1,6}

3 ¹College of Global Change and Earth System Science, Beijing Normal University,
4 Beijing, China

5 ²Arctic Centre, University of Lapland, Rovaniemi, Finland

6 ³CAS Center for Excellence in Tibetan Plateau Earth Sciences, Beijing, 100101, Chin.

7 ⁴Center for Disaster Mitigation and Climate Change, Institut Teknologi Sepuluh
8 Nopember, Surabaya, Indonesia

9 ⁵Department of Statistics, Institut Teknologi Sepuluh Nopember, Surabaya, Indonesia

10 ⁶State Key Laboratory of Earth Surface Processes and Resource Ecology, Beijing
11 Normal University, Beijing, China

12 *Correspondence to:* john.moore.bnu@gmail.com

13

14 Short summary

15 The Indonesian Throughflow is an important pathway connecting the Pacific and Indian
16 Oceans. Solar dimming and sulfate aerosol injection geoengineering will affect the
17 water volumes transported in future – but so will increasing greenhouse gases.
18 Geoengineering with sulfate aerosols affects winds more than simply “shading the sun”
19 and reduces the water transport more – similar as we simulate for unabated greenhouse
20 gas emissions.

21

22 **Abstract**

23 The Indonesia Throughflow (ITF) is the only low-latitude channel between the Pacific
24 and Indian oceans, and its variability has important effects on global climate and
25 biogeochemical cycles. Climate models consistently predict a decline in ITF transport
26 under global warming, but it has not yet been examined under solar geoengineering
27 scenarios. We use standard parameterized methods for estimating ITF: the Amended
28 Island Rule and Buoyancy Forcing, to investigate ITF under the SSP2-4.5 and SSP5-
29 8.5 greenhouse gas scenarios, and the geoengineering experiments G6solar and



30 G6sulfur that reduce net global mean radiative forcing from SSP5-8.5 levels to SSP2-
31 4.5 levels using solar dimming and sulfate aerosol injection strategies. Six model
32 ensemble mean projections for 2080 - 2100 relative to historical ITF are reductions of
33 19% under the G6solar scenario and 28% under the G6sulfur scenario which compare
34 with reductions of 23% and 27% under SSP2-4.5 and SSP5-8.5. Thus, significant
35 weakening of the ITF occurs under all scenarios, but G6solar closer approximates
36 SSP2-4.5 than does G6sulfur. In contrast with the other three scenarios which show
37 only reductions in forcing due to ocean upwelling, the G6sulfur experiment shows a
38 large reduction in ocean surface wind stress forcing accounting for 47% (38%~65%
39 across model range) of the decline of total ITF transport. There are also reductions in
40 deep-sea upwelling in extratropical western boundary currents.

41

42 **1. Introduction**

43 The Indonesian Throughflow (ITF) is an important part of the global thermohaline
44 circulation (Gordon, 1986; Lee et al., 2002; Sprintall et al., 2009). The ITF brings about
45 of 15 Sv (1 Sv = $10^6 \text{ m}^3/\text{s}$; ~10.7 to ~18.7 Sv during the INSTANT Field Program, 2004-
46 2006) of warm and fresh water from the Pacific to the Indian Ocean (Sprintall et al.,
47 2009). Since the ITF is the only ocean pathway in the tropics between the Pacific and
48 Indian Oceans it is the key to heat and water volume transport between them (Godfrey,
49 1996; Talley, 2008). The ITF also plays an important role in regulating global climate
50 and biogeochemical cycles (Ayers et al., 2014; Hirst and Godfrey, 1994), for example
51 in the supply of iron in the equatorial upwelling, maintaining biological production in
52 the equatorial eastern Pacific (Gorgues et al., 2007).

53

54 The ITF is fed by the Mindanao Current and the New Guinea Coast Undercurrent
55 (Figure 1) and, to a lesser extent, parts of the low-latitude Pacific Western Boundary
56 Current (WBC) that flows toward the equator (Godfrey, 1996; Lukas et al., 1996). The
57 ITF provides a compensating flow for the Agulhas current leakage from the Indian
58 Ocean to the South Atlantic Ocean, and may be said to flush Indian Ocean thermocline



59 waters southward by boosting the Agulhas current (Durgadoo et al., 2017; Gordon,
60 2005).

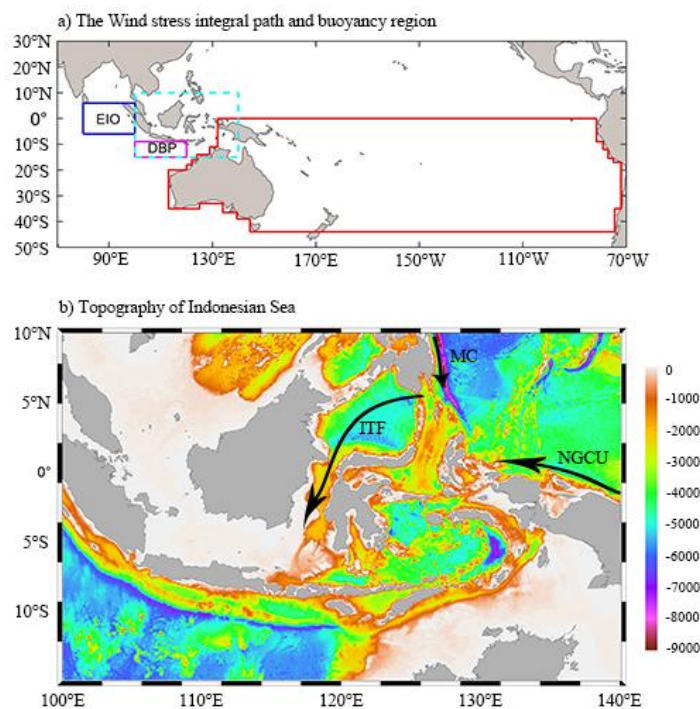
61

62 The interannual and decadal variability of the ITF transport is influenced by surface
63 winds in the Pacific and Indian Oceans (Feng et al., 2011; Meyers, 1996). Wyrski (1987)
64 noticed that the pressure gradient between the Pacific and Indian Oceans dominates the
65 ITF flux, and hence that sea level is a good indicator of upper-ocean ITF transport. The
66 largest volume flux is in July-August and the lowest in January-February.

67

68 Model simulations consistently project that ITF transport will be weakened by
69 increased greenhouse gas (GHG) forcing (Feng et al., 2012; Hu et al., 2015; Sen Gupta
70 et al., 2021; Vecchi and Soden, 2007). The driving force is the weakening of the Pacific
71 trade winds under global warming in the 21st century which then weaken the Mindanao
72 Current, the main inflow route of the ITF (Alory et al., 2007; Duan et al., 2017; Sen
73 Gupta et al., 2012).

74



75

76 Figure 1. (a) The red line is the wind stress integral path for the Island Rule, The Downstream Buoyant
77 Pool (magenta box) and Equatorial Indian Ocean (blue box) where the density difference is the main
78 index to calculate the ITF transport by buoyance forcing. (b) Inset defined by the cyan dotted line in the
79 panel (a) showing the offshore bathymetry in the maritime continent (ETOPO Global Relief Model,
80 (Amante and Eakins, 2009)) and the Mindanao Current (MC), and the New Guinea Coast Undercurrent
81 (NGCU) paths contributing to the ITF.

82

83 Analyzing the water flux through the many shallow channels in the Indonesian
84 archipelago is challenging, and many of these channels are not resolved in simulations
85 (Figure 1). This motivates the use of alternative methods of estimating ITF. Godfrey
86 (1989) created the Island Rule to estimate flux based on Sverdrup theory (Sverdrup,
87 1947) analysis of Pacific wind stress. More recently, analysis of climate models
88 revealed the importance of deep ocean circulation to the reduction of ITF transport
89 under GHG forcing. Sen Gupta et al. (2016), and Feng et al. (2017) proposed the
90 Amended Island Rule that modifies the Island Rule to include the estimated net Pacific



91 upwelling contribution to ITF based on high-resolution ocean general circulation
92 modelling. Earlier, Andersson and Stigebrandt (2005) had proposed that buoyancy
93 forcing was more important than wind forcing in driving the ITF, and estimated the ITF
94 variability from the baroclinic outflow of the Downstream Buoyant Pool (DBP) that
95 extends over much of the North Australian Basin (Figure 1). Hu and Sprintall (2016)
96 used this method with reanalysis products to produce ITF interannual variability in
97 good agreement with the observed volume transports (2004–2006) from the INSTANT
98 mooring array transport (Sprintall et al., 2009), although the average transport was
99 smaller than the observed transport. Changes in buoyancy forcing that may affect
100 volume transport of the ITF on decadal scales under changing climate is therefore a
101 concern.

102

103 Solar Radiation Modification (SRM) geoengineering is designed to reduce the solar
104 radiation reaching the surface of the earth and slow down climate warming due to GHG
105 forcing (Shepherd, 2009). Since SRM shortwave forcing has different spatial and
106 temporal variability than longwave forcing, it can only imperfectly offset the climate
107 change caused by the increase of GHGs. In this article we focus on two styles of SRM:
108 reduction of the solar constant to mimic the effect of a sunshade, called solar dimming
109 (SD); and stratospheric aerosol injection (SAI), specifically with injection of sulfate
110 aerosol in the tropical lower stratosphere (Kravitz et al., 2015). These styles of SRM
111 are known to produce over-cooled tropical oceans and under-cooled poles relative to
112 global mean temperatures, but these particular methods are unlikely to ever be done,
113 with more sophisticated injection and monitoring approaches able to remove these
114 temperature biases (MacMartin and Kravitz, 2016). Simulated tropical circulation
115 systems are impacted under both GHG and solar geoengineering scenarios; under SD
116 the seasonal movement of the intertropical convergence zone is reduced relative to
117 GHG climates (Smyth et al., 2017), and both the Hadley and Walker circulations are
118 different from the historical (Guo et al., 2018). North Atlantic hurricane numbers and
119 intensity relative to GHG-only climates are reduced under SAI (Moore et al., 2015),
120 but there are differences between tropical basins in expected tropical cyclogenesis



121 potential and significant differences in simulations between climate models (Wang et
122 al., 2018). Potential energy available for extratropical storms is also consistently
123 reduced under SRM relative to GHG forcing (Gertler et al., 2020).

124

125 Little research to date has been done on ocean circulation under SRM, with only the
126 Atlantic Meridional Overturning Circulation (AMOC) having been studied in depth
127 (Hong et al., 2017; Moore et al., 2019; Muri et al., 2018; Tilmes et al., 2020; Xie et al.,
128 2022). Both GHG forcing alone, and with SRM, produce a weakening of AMOC
129 relative to present day, mainly in response to the change of ocean-atmosphere heat flux
130 in the North Atlantic, with little influence from the changes of freshwater flux and wind
131 stress (Hong et al., 2017; Xie et al., 2022). AMOC is less weakened under SRM than
132 with GHG forcing alone and the AMOC declines seen under GHG forcing are
133 consistently reversed by SRM towards present day patterns (Moore et al., 2019; Muri
134 et al., 2018; Tilmes et al., 2020).

135

136 In this study, we will explore the impact of SRM on the change of ITF in the 21st
137 century, explore the drivers of these changes, and consider the differences between pure
138 GHG climates representing moderate mitigation (SSP2-4.5) and no mitigation (SSP5-
139 8.5); and with solar dimming (G6solar) and stratospheric aerosol injection (G6sulfur)
140 forms of SRM geoengineering.

141

142 **2. Climate Models and Scenarios**

143 The Intergovernmental Panel on Climate Change (IPCC) Shared Socioeconomic
144 Pathways (SSPs) are scenarios defined by radiative forcing goals to be achieved
145 through various climate mitigation policy alternatives (Kriegler et al., 2012; van Vuuren
146 et al., 2011). The climate model simulation results under the SSPs are being performed
147 as part of the Coupled Model Intercomparison Project Phase 6 (CMIP6). We used
148 CMIP6 historical simulation during 1980-2014 (Eyring et al., 2016) and two GHG
149 scenarios during 2015-2100: SSP5-8.5, an unmitigated GHG emission scenario which



150 raises mean global radiative forcing by 8.5 W/m^2 over pre-industrial levels at 2100;
151 and SSP2-4.5 designed to reach peak radiative forcing of 4.5 W/m^2 by mid-century
152 (O'Neill et al., 2016). We use the Geoengineering Model Intercomparison Project Phase
153 6 (GeoMIP6) G6sulfur and G6solar scenarios during 2020-2100 (Kravitz et al., 2015).
154 The G6sulfur experiment specifies using SAI to reduce the net anthropogenic radiative
155 forcing constantly during the 2020-2100 period from the SSP5-8.5 to the SSP2-4.5 level,
156 while G6solar does the same using SD (Kravitz et al., 2015). The two SRM methods
157 produce significantly different surface climates, with differences from SSP2-4.5 being
158 larger and more spatially variable under G6sulfur than G6solar (Visoni et al., 2021).
159 While the G6 scenarios are not particularly realistic, they provide a usefully large SRM
160 and GHG signal for a multi-model ensemble of CMIP6 generation models to generate
161 robust findings.

162

163 We used monthly data from the first realization in each scenario from all six Earth
164 System Models (ESM; Table 1) that have performed the CMIP6 and GeoMIP6
165 scenarios to estimate the ITF transport. The variable fields we use are zonal and
166 meridional wind stress (τ_{uu} and τ_{uv}), sea water vertical velocity (w_o), sea water
167 salinity and temperature (so and θ_{tao}) and all fields were interpolated onto a common
168 $0.5^\circ \times 0.5^\circ$ grid.

169

170 **Table 1**

171 *Earth System Models (ESMs) Used in This Study*

Model	Atmospheric Resolution (long \times lat)	Ocean Resolution (long \times lat)	Reference
CESM2-WACCM	288 \times 192	320 \times 384	(Danabasoglu et al., 2020)
CNRM-ESM2-1	256 \times 128	362 \times 294	(Séférian et al., 2019)
IPSL-CM6A-LR	144 \times 143	320 \times 384	(Boucher et al., 2020)
MPI-ESM1-2-HR	384 \times 192	802 \times 404	(Mauritsen et al., 2019)
MPI-ESM1-2-LR	192 \times 96	256 \times 220	(Mauritsen et al., 2019)
UKESM1-0-LL	192 \times 144	360 \times 330	(Sellar et al., 2019)



172

173 **3. Methods**

174 3.1 Island Rule

175 In the Sverdrup balance, ocean current acceleration and friction are neglected, and wind
176 stress curl is the driving force of large-scale ocean circulation (Sverdrup, 1947). The
177 “Island Rule” (Godfrey, 1989) uses the Sverdrup balance to calculate the net total flow
178 through a region by the integral of the wind stress on a specific closed path. This is a
179 simple and more efficient way of estimating the long-term magnitude and interannual
180 variability than direct observations of flow through the complex channel topography
181 and equator spanning Indonesian archipelago (Godfrey, 1996). Models have verified
182 that the Island Rule can capture the decadal variability of the ITF transport (Feng et al.,
183 2011).

184

185 The original Island Rule assumes that the ocean is dormant below a moderate depth, Z ,
186 below which there is no motion (Sverdrup, 1947). The ITF transport is determined by
187 the integral of wind stress along the path from the southern tip of Australia, eastwards
188 to South America, following the coastline to the latitude line of the northwestern tip of
189 Papua New Guinea (PNG) and then traces the west coast of Australia back to the
190 starting point (Figure 1a):

$$191 \quad T_{ITF} = \frac{1}{f_N - f_S} \oint \frac{\tau^l}{\rho_0} dl \quad (1)$$

192 where, f_N and f_S are the Coriolis parameter at the equator and 44°S, respectively. τ^l is
193 the along route wind stress component. ρ_0 is the mean sea water density.

194

195 3.2 Amended Island Rule

196 Studies have suggested that a decline in ITF under GHG forcing was due to both the
197 weakening of trade winds in the Pacific, and the impact of the deep ocean circulation
198 change (Feng et al., 2012; Hu et al., 2015). Sen Gupta et al. (2016) used a climate model
199 to attribute GHG-forced decrease of the ITF transport to weakening of deep Pacific



200 upwelling. Feng et al. (2017) estimated the contribution of deep ocean upwelling from
201 the Pacific north of 44°S to produce the Amended Island Rule:

$$202 \quad T_{ITF} = \frac{1}{f_N - f_S} \oint \frac{\tau^l}{\rho_0} dl + \iint_{pacific} w_z ds \quad (2)$$

203 where, w_z is the vertical velocity of the Pacific at 1500 m depth. The Amended Island
204 Rule was verified with a near-global eddy-resolving ocean model simulation, and found
205 to well-estimate the interannual to decadal, as well as centennial variabilities of the ITF
206 transport (Feng et al., 2017). Here we describe the ITF using the Amended Island Rule,
207 and its component parts which are the wind driven Sverdrup balance, and the Pacific
208 upwelling.

209

210 3.3 Buoyancy Forcing

211 Sea levels in the Pacific and Indian Oceans have been used to estimate the ITF transport
212 in most studies (Clarke and Liu, 1994; Potemra et al., 1997; Susanto and Song, 2015).
213 Buoyancy accounts for high steric sea level in the North Pacific (Stigebrandt, 1984),
214 and should also drive the Indo-Pacific pressure gradient. A pool of low-density water
215 (the DBP) originating in the North Pacific is formed in the eastern Indian Ocean
216 between the Indonesian islands and northwestern Australia (Figure 1a). The sea level
217 drop between Indian and Pacific Oceans occurs essentially at the sharp boundary of the
218 DBP and is the source of buoyancy forcing (Andersson and Stigebrandt, 2005). In the
219 DBP region, the long-term difference between the westward and eastward transport
220 along the northern and southern flanks of the pool is the ITF transport.

221

222 The geostrophic transport in the DBP is related to denser water in the eastern equatorial
223 Indian Ocean (EIO):

$$224 \quad Q_\lambda = \frac{gH^2\Delta\rho}{2f_\lambda\rho_0} \quad (3)$$

$$225 \quad ITF = Q_{\lambda_N} - Q_{\lambda_S} \quad (4)$$

226 where, g is acceleration due to gravity, H is the penetration depth of the DBP (set by
227 (Andersson and Stigebrandt, 2005) as 1200 m), f_λ is the Coriolis parameter at latitude



228 λ , ρ_0 is the reference density at 1200 m, The northern (λ_N) and southern (λ_S) boundary
229 latitudes of the DBP are 10°S and 16°S respectively. $\Delta\rho$ is the density difference
230 between the DBP region (9°S–15°S, 100°E–120°E) and the EIO region (6°N–6°S, 80°
231 E–100°E). Hu and Sprintall (2016) verified the use of DPB and EIO to calculate $\Delta\rho$
232 with observations.

233

234 **4. Transport and Geoengineering**

235 4.1 ITF Transport

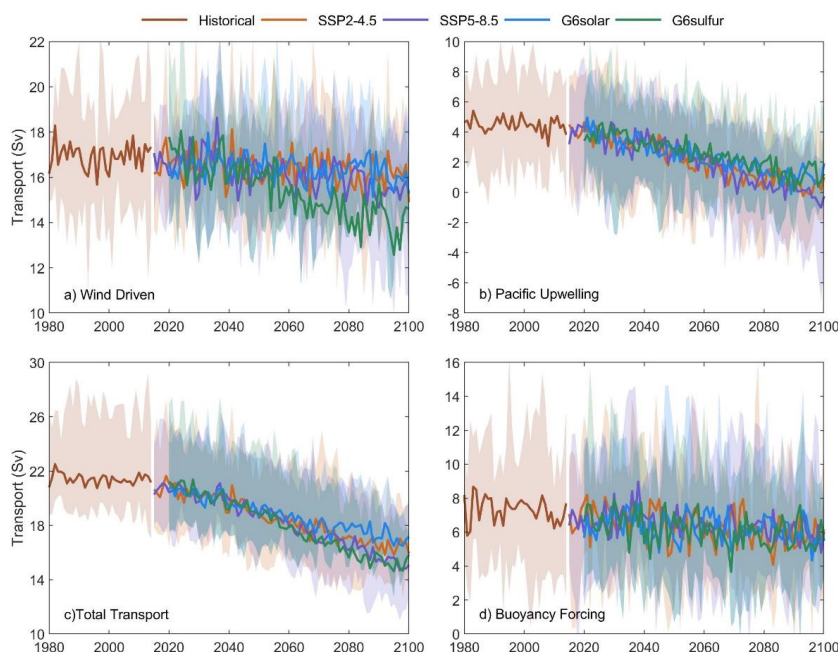
236 The multi-model ensemble mean wind driven ITF transport is ~16.9 Sv with the Pacific
237 upwelling north of 44°S contributing ~4.5 Sv in the historical period (Figure 2). This
238 compares with observational estimates of about 15 Sv during 2004-2006 (Sprintall et
239 al., 2009) and the multi-model ensemble (total 22 CMIP5 models) mean is 15.2 Sv
240 during 1900-2000 (Sen Gupta et al., 2016). Under SSP2-4.5 during 2015 - 2100, the
241 wind-driven and Pacific upwelling contributions to ITF transport are not much different
242 from those under SSP5-8.5. The wind driven volume ITF transport has no trend for the
243 SSP scenarios, while the upwelling contributions has clear downward trends in all
244 scenarios. This trend appears to be consistent, despite differences in estimated transport
245 across models (Figure S1). Thus the decline in future ITF transport in future GHG
246 climates was explained by (Feng et al., 2017) as due to weakening of the Pacific
247 upwelling on centennial timescales while wind-driven processes had no impact on long
248 timescales.

249

250 During the last 20 years of the 21st century, the simulated ITF transport under the
251 Amended Island Rule is 27% lower under SSP5-8.5 (Figure 2c), with Pacific upwelling
252 decline accounting for 76% of the total reduction. Both wind driven and upwelling
253 contributions to ITF transport are slightly higher under SSP2-4.5 than under SSP5-8.5
254 during the same period, but the differences are small over the whole 2015-2100 period.
255 The total ITF transport is reduced by 23% under SSP2-4.5 during the period of 2080-



256 2100 relative to the historical period, with 87% reduction in the Pacific upwelling
257 contributions (59%~244% cross ESM range) and with the wind driven component only
258 dropping by 5% (-2%~9% range). The reductions under SSP5-8.5 for upwelling and
259 wind driven components are respectively 97% (60%~305%) and 8% (1%~19%).
260
261 The multi-mean ITF transport simulated by buoyancy forcing is 7.3 Sv in the historical
262 period, which is less than that by wind driven and only half the transport observed
263 during INSTANT (Sprintall et al., 2009), and there is large across-model variability
264 (Figure S2). Under the two SSPs scenarios, the difference in ITF transport is small with
265 no obvious trend during 2015-2100. The buoyancy driven estimation method can
266 capture the interannual variability of ITF transport, but it does not perform well on
267 centennial timescales (Hu and Sprintall, 2016), where it is similar to the wind driven
268 estimation scheme.
269



270
271 **Figure 2.** Six ESM ensemble mean ITF components under different scenarios, shadings show the
272 across-model range. (a) Sverdrup balance wind driven component. (b) Pacific upwelling north of 44°S.



273 (c) Total ITF under the Amended Island Rule (eqn 2). (d) ITF transport by buoyancy forcing. Individual
274 ESM results are shown in Figure S1.

275

276

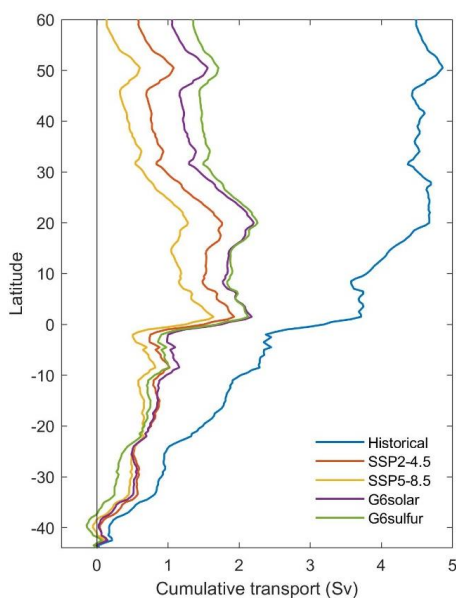
277 SAI and SD geoengineering methods have different effects on wind driven and
278 upwelling contributions to ITF transport (Figure 2a,b). Under the G6solar and G6sulfur
279 scenarios, the total ITF transport is reduced by 19% and 28% respectively during 2080
280 - 2100 relative to the historical period, of which the wind-driven ITF transport is
281 reduced by 4% and 16%, and the upwelling transport volume is reduced by 76% and
282 70%. Under G6sulfur, the wind driven ITF transport has a clear downward trend in
283 contrast with the other three climate scenarios (Figure 2a). Each ESM also shows
284 consistency in the relative declines under the four future climates (Figure S1a). The
285 decline of wind driven transport accounts for 47% (38%~65%) of the decline of total
286 ITF transport under G6sulfur during 2080-2100, and its ensemble mean wind driven
287 transport volume is even lower than that under SSP5-8.5. The ensemble mean ITF
288 transport by buoyancy forcing is less under the two G6 scenarios than under the two
289 SSP scenarios; the minimum is under G6sulfur and the maximum is under SSP5-8.5
290 (Figure 2d), which is different from the transport change calculated using the wind
291 driven and upwelling contributions.

292

293 The decline in ITF transport via upwelling in future relative to present under all
294 scenarios is illustrated in Figure 3. During the historical period, the zonally integrated
295 upwelling contributions to ITF transport in the Pacific Ocean steadily accumulate when
296 progressing from southern latitudes until about 20°N. Latitudes further north make little
297 contribution and accumulated upwelling is then fairly constant. This pattern changes in
298 all future climate scenario simulations. The Pacific upwelling contributions to transport
299 volume accumulate steadily, but slower with latitude than under the historical
300 simulation, until to just north of the equator (2°N), and then, after a small decrease
301 rapidly accumulates over a few degrees of latitude. North of 20°N, the integrated



302 upwelling declines. Between 44°S and 15°S, the zonal cumulative transport curves
303 under SSP2-4.5 and G6solar are relatively similar. Figure 3 depicts the integrated
304 upwelling under the G6sulfur scenario transitions from the smallest of the four future
305 scenarios between 44°S and 20°S to the largest a few degrees north of the equator.
306



307
308 **Figure3.** Multi-model ensemble mean zonal cumulative transport by Pacific upwelling north of 44°S
309 during the historical simulation (1980-2014) and under the four future scenarios (2080-2100).

310

311 4.2 ITF by geoengineering type

312 4.2.1 Wind stress

313 Godfrey et al. (1993) suggested that the Indonesian throughflow originates in the South
314 Pacific, where the South Equatorial Current retroflects into the North Equatorial
315 Countercurrent and enters the Indonesian Sea via the Mindanao Current. Wind stress
316 curl is determined by the components of the wind stress vector and drives the ocean
317 circulation (Gill and Adrian, 1982). In the South Pacific under the SSP2-4.5 scenario
318 during 2080-2100, the wind stress curl in the middle latitudes is stronger than in the
319 historical period, while that at low latitudes and along the west coast of South America



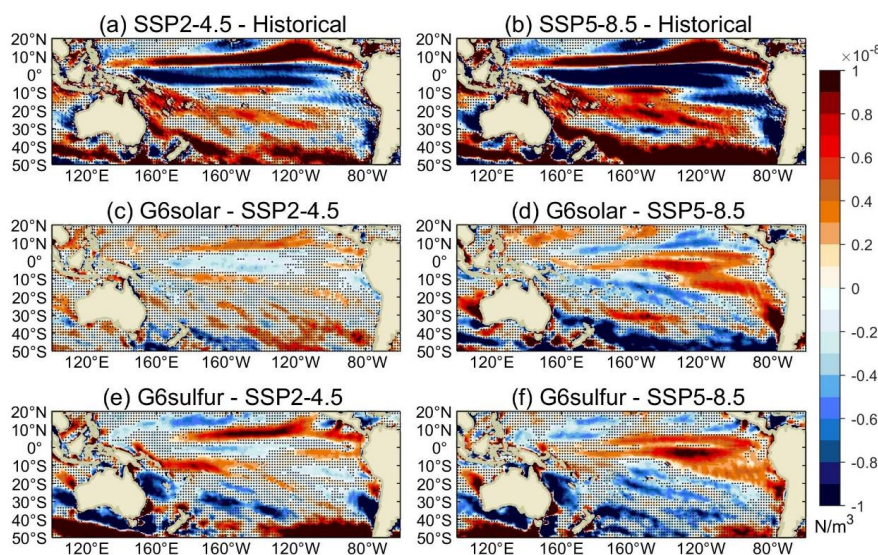
320 it is weaker than in the historical period (Figure 4a). The SSP5-8.5 scenario anomalies
321 relative to the historical period are similar but extend over a larger region and have
322 larger amplitude (Figure 4b). Net ITF transport volume under SSP5-8.5 is lower than
323 the historical, which is consistent with the difference in wind stress curl between the
324 simulations. There is no significant difference in wind stress curl between G6solar and
325 SSP2-4.5 in mid latitudes, and the difference in low latitudes is relatively small (Figure
326 4c). The wind stress curl under G6solar is slightly weaker at mid latitudes and slightly
327 stronger at low latitude than with SSP5-8.5 (Figure 4d). Differences between wind
328 stress curl under G6sulfur and SSP2-4.5 scenarios are mainly in the mid latitudes, near
329 the equator and the west coast of South America (Figure 4e), which are related to the
330 wind driven ITF transport changes. In contrast, the significant differences between the
331 wind stress curl under G6sulfur and SSP5-8.5 are mainly in the northeast of the South
332 Pacific, and the wind stress curl under G6sulfur is stronger than that under SSP5-8.5
333 (Figure 4f). The wind stress curl at the inlet of the ITF is significantly weakened under
334 the G6sulfur scenario compared with the two SSPs scenarios.

335

336

337

338



339

340 **Figure 4.** The multi-model mean differences in wind stress curl (a) SSP2-4.5 and historical, (b)
341 SSP5-8.5 and historical, (c) G6solar and SSP2-4.5, (d) G6solar and SSP5-8.5, (e) G6sulfur and SSP2-
342 4.5, (f) G6sulfur and SSP5-8.5. The historical period is 1980-2014, and the future scenarios period is
343 2080-2100. Stippling indicates regions where differences are not significant at the 95% level by the
344 Wilcoxon signed-rank test.

345

346 The multi-model average ITF transport between G6 scenarios and SSPs scenarios
347 shows significant differences during 2020-2100 (Table 2). Differences in wind-induced
348 ITF transport from SSP2-4.5 are smallest with G6solar (Table 2) and are not
349 significantly different in every ESM (Table S1). Differences between SSP5-8.5 and
350 G6solar are the same sign for wind and upwelling forcings, contributing to larger
351 differences in the amended island rule total transport. With G6sulfur, differences in
352 wind and upwelling forcing differences from SSP5-8.5 are oppositely signed, and the
353 net transport difference is quite small, but still significant for the six models ensemble.
354 Differences in the ITF defined by buoyancy are only significant for G6sulfur-SSP5-8.5.

355

356

357 **Table 2**



358 The differences in ITF Transport (2020-2100)^a and its components; TRN_{wind} is the ITF transport derived
359 from Island Rule; $TRN_{Upwelling}$ is the area integral of Pacific upwelling rate at 1500m; TRN_{Total} is the ITF
360 transport calculating by Amended Island Rule; $TRN_{Buoyancy}$ is the ITF transport by buoyancy forcing. Unit:
361 Sv ($1Sv = 10^6 m^3/s$)

362

Differences	TRN_{wind}	$TRN_{Upwelling}$	TRN_{Total}	$TRN_{Buoyancy}$
G6solar – SSP2-4.5	0.02	0.33	0.35	-0.06
G6sulfur – SSP2-4.5	-0.96	0.53	-0.44	-0.21
G6solar – SSP5-8.5	0.23	0.4	0.63	-0.15
G6sulfur – SSP5-8.5	-0.75	0.59	-0.16	-0.3
G6sulfur – G6solar	-0.98	0.19	-0.79	-0.15

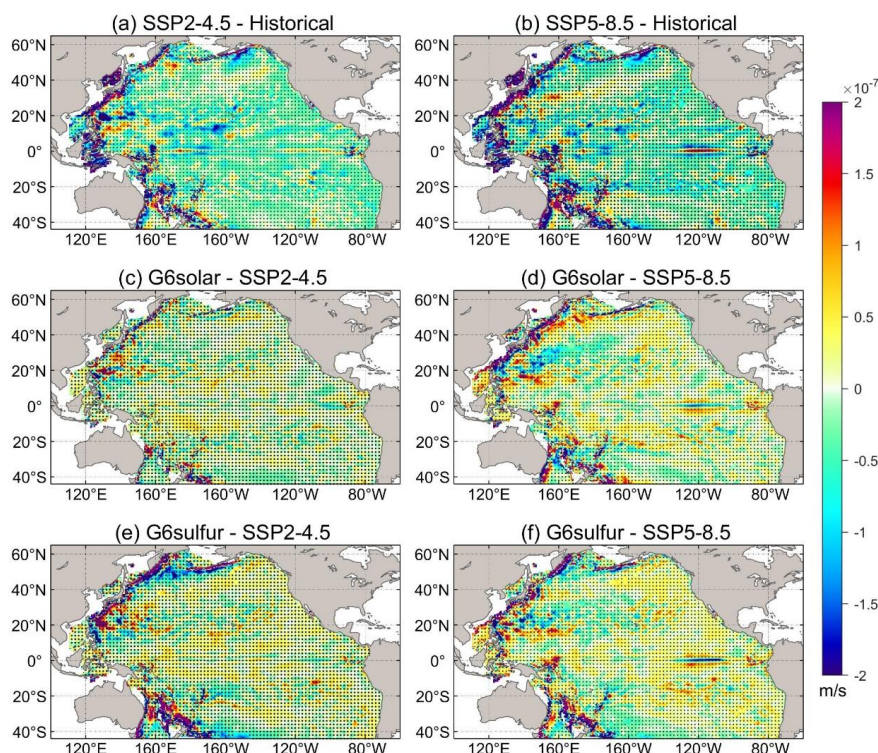
363

364 ^aThe end dates of the G6solar and G6sulfur of MPI-ESM1-2-HR are 2099 and 2089, respectively, and those of MPI-ESM1-2-LR
365 are both in 2099. Values in bold are significant at the 95% level according to the Wilcoxon signed-rank test.

366

367 4.2.2 Upwelling

368 The spatial pattern of upwelling velocity at 1500 m in the Pacific under present day
369 conditions is for strong upwelling at the equator, weak upwelling in the interior, and
370 mixed up- and down-welling along the ocean boundaries (Feng et al., 2017). Spatial
371 patterns of upwelling changes are shown in Figure 5. The western boundary currents
372 are an important source of ITF gradient differences in wind stress that drive ocean
373 currents (Hu et al., 2015), and these gradients remain present at great depth in the
374 western boundary current region. Much of the ocean shows no significant changes in
375 upwelling velocity, but the western boundaries differ significantly from the historical
376 in both SSP scenarios (Figure 5a,b), and under SSP5-8.5 there is also a significant
377 upwelling in the equatorial eastern Pacific. The difference of upwelling velocity
378 between G6solar and SSP2-4.5 scenarios is insignificant almost everywhere (Figure
379 5c), while differences from SSP5-8.5 are significant mainly along the extratropical
380 western ocean boundaries. G6sulfur differences from the SSP scenarios are clearly
381 larger than those for G6solar, and are greater in the extratropics than in the tropics.
382 The pattern of changes in upwelling anomalies for G6sulfur-SSP2-4.5 is similar but of
383 opposite sign to G6solar-SSP5-8.5 (Figure 5e), while differences for G6sulfur and
384 SSP5-85 are similar or slightly smaller than differences from SSP2-4.5 (Figure 5f).



385
386 **Figure 5.** Changes in the multi-model ensemble mean upwelling velocity at 1500m (blue indicates
387 increased upwelling, red indicates relative downwelling) for (a) SSP2-4.5 and historical, (b) SSP5-8.5
388 and historical, (c) G6solar and SSP2-4.5, (d) G6solar and SSP5-8.5, (e) G6sulfur and SSP2-4.5, (f)
389 G6sulfur and SSP5-8.5. The historical period is 1980-2014, and the future scenarios period is 2080-2100.
390 Stippling indicates regions where differences are not significant at the 95% level by the Wilcoxon signed-
391 rank test.

392

393

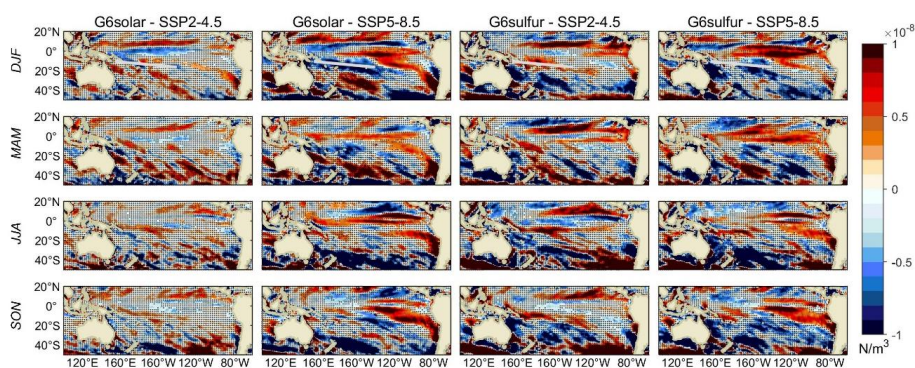
394 4.2.3 Seasonality

395 Seasonal patterns in ITF are important and reflect changes in position of the two main
396 precipitation convergence zones across the region. Model simulations show that
397 decreases in ITF transport in April-May and October-November, and their recovery are
398 due to the upper ocean changes associated with the Rossby waves in the Pacific Ocean,
399 and that the seasonal ITF transport is closely related to wind variations in the Pacific



400 and Indian Oceans (Shinoda et al., 2012). The South Pacific convergence zone (SPCZ)
401 is a strong rainfall and convection zone extending from the equator to the subtropical
402 South Pacific, which is generated by the low-level convergence between the northeast
403 trade wind and weaker westerly wind (Vincent, 1994). The SPCZ is clearest in
404 December-February (DJF), the Southern hemisphere summer, and is marked in the top
405 row of Figure 6. The annual wind stress curl differences between G6solar and SSP2-
406 4.5 are small, but the seasonal variation difference in some regions is significant. Under
407 G6solar, compared with SSP2-4.5, the wind stress curl near the equator is weakened in
408 DJF. In March to May (MAM), the wind stress curl in the middle and low latitudes of
409 the southern hemisphere is generally enhanced. SSP5-8.5 has significantly lower wind
410 stress curl in the SPCZ region relative to G6solar in DJF. In MAM, their differences are
411 mainly in the mid latitudes. From June through November (JJA and SON), wind stress
412 curl under SS5-8.5 is significant lowered between 30 °S and 50 ° S. In contrast G6sulfur
413 shows significant increase in the SPCZ region in DJF, and a significant decrease the
414 south of SPCZ region in JJA relative to SSP2-4.5. There are large differences in the
415 ocean northeast of New Zealand with the sign reversing from MAM to JJA. Differences
416 between G6sulfur and SSP5-8.5 are not very much bigger than from SSP2-4.5, and the
417 patterns are quite similar. The wind stress curl in the SPCZ region and its extension
418 southeastwards is significantly weakened under G6sulfur relative to both SSP scenarios
419 in DJF. In JJA the region with decrease in wind stress curl east from New Zealand is
420 slightly larger relative to SSP5-8.5 and SSP2-4.5.

421



422



423 **Figure 6.** Seasonal ESM ensemble mean spatial differences (G6solar – SSP2-4.5, G6solar – SSP5-8.5,
424 G6sulfur - SSP2-4.5, G6sulfur – SSP5-8.5) of the wind stress curl during 2080-2100. The white lines in
425 each panel of the top row marks the mean the position of the South Pacific Convergence Zone (SPCZ)
426 in DJF based on the CMIP6 multi-model mean (Brown et al., 2020). Stippling indicates regions where
427 differences are not significant at the 95% level by the Wilcoxon signed-rank test, significant differences
428 are larger than $|0.5 \times 10^{-8}| \text{ Nm}^{-3}$

429
430

431 **5. Summary and Discussion**

432 The wind driven ITF transport estimated using the six CMIP6 models historical
433 scenario is well within the range of 11-20 Sv, found from 22 CMIP5 models (Sen Gupta
434 et al., 2016). These model estimates tend to slightly overestimate ITF compared with
435 observed ITF (15 ± 3 Sv) since Godfrey’s Island Rule ignores friction due to real ocean
436 topography (Feng et al., 2005; Wajsowicz, 1993). The rather large interannual and
437 decadal variations in the ITF (amounting to several Sv) are mainly influenced by the
438 Pacific and Indian Ocean winds. There is an observed relationship between ITF
439 transport and the El Niño-Southern Oscillation (ENSO), with stronger transport during
440 La Niña and weaker transport during El Niña, with ITF variability lagging ENSO
441 variability by 8-9 months (England and Huang, 2005; Meyers, 1996). No effects of
442 ENSO on ITF transport are obvious in our results as the models ENSO variability is not
443 synchronized or tuned to the real world but exists as an emergent property of each ESM
444 (Rezaei et al., 2022).

445

446 The six ESM we use concur on weakening of ITF transport in all future scenarios. That
447 is SRM cannot restore the ITF to its historic levels. This contrasts somewhat to the
448 changes simulated in the AMOC under SRM with GHG forcing, where it seems that
449 SRM can almost reverse the slow down in AMOC induced by GHG forcing (Muri et
450 al., 2018; Tilmes et al., 2020; Xie et al., 2022). This illustrates the important regional
451 variability of response to SRM, and the differences between the wind-driven ITF and



452 the surface heat flux driver of AMOC.

453

454 Weakening of the ITF transport appears in all future scenarios, both with pure GHG
455 forcing, and combining GHG and SRM strategies. The ITF transport changes are
456 defined almost totally (around 90%) by significant differences in Pacific upwelling
457 (Figure 2a and 2b). This is consistent with the conclusion that the weakening trend of
458 ITF under global warming predicted by high-precision ocean models is not directly
459 related to the change of Pacific trade winds but to the reduction of Pacific deep-sea
460 upwelling (Feng et al., 2017). On centennial scales, the decrease of the net deep ocean
461 upwelling in the tropics and the South Pacific, especially the changes in the western
462 boundary current system is what determines ITF transport. Buoyancy forcing can only
463 estimate the interannual variation of the ITF, and our study supports the utility of the
464 Amened Island Rule in estimating centennial changes in ITF transport.

465

466 Sen Gupta et al. (2021) note that projected weakening of the ITF and differences
467 between ESM can be explained by changes in large-scale surface winds. This contrasts
468 with our findings where changes in wind driven transport are not significantly different
469 between models, but instead upwelling in the extratropical western boundary zones
470 dominates changes between scenarios. However, western boundary currents are deep
471 and narrow and differ from the shallow and wide eastern boundary currents. The tropics
472 experience weaker (and reversed) trade winds from those that dominate the
473 extratropical regions. The geographical differences in upwelling suggest that wind
474 changes are driving the overall changes in ITF via upwelling regions, and so in effect
475 supporting the conclusion of Sen Gupta et al. (2021) that differences in future surface
476 winds explain most of the differences in future large scale current systems.

477

478 SSP2-4.5 global radiative forcing was the design target of the G6 experiments despite
479 GHG concentrations being at SSP5-8.5 levels. The difference in wind stress curl
480 between G6solar and SSP2-4.5 indicates that the SD experiment performs better at
481 reversing GHG induced changes in Pacific wind than G6sulfur. The G6sulfur SAI



482 experiment leads to a significant change in the winds in mid and low latitude Pacific
483 Ocean, which results in even lower estimated ITF transport than under the high GHG
484 SSP5-8.5 forcing alone. Furthermore, G6sulfur also impacts deep ocean upwelling
485 especially in the extratropical western boundary current region, such that the ITF
486 transport during the 21st century under the G6sulfur scenario is slower than that under
487 the G6solar scenario. The G6 scenarios do not affect low latitude western boundary
488 currents and upwelling, for example the upwelling near the Mindanao current is
489 unaffected while the upwelling along the Kuroshio current is apparently displaced in
490 both G6 experiments. The ITF transport under the SD experiment was stronger than
491 under the SAI experiment and even higher than its target SSP2-4.5 scenario level at the
492 end of the 21st century.

493
494 Changes in circulation in the future will have important impacts on aquatic ecology and
495 fisheries (Dubois et al., 2016). In fact, the population in Indonesia's coastal areas,
496 especially those in the islands through which the ITF passes, are highly dependent on
497 fisheries and hence, the changes in ITF under both pure GHG and mixed GHG and
498 SRM scenarios will have important local implications on the livelihood and ways of
499 life of the local populations. Seasonal variations in ITF transport reflect important
500 processes in the tropical convergence zones, and these are clearly impacted by all 4
501 future scenarios in generally subtle ways. But the largest differences are seen between
502 the two most challenging scenarios to simulate – SSP5-8.5 and G6sulfur. Despite the
503 large size of perturbation that these forcings apply in the simulations, and the
504 differences between climate models in parameterizing the SAI schemes, the finding are
505 rather robust in the changes of winds in all seasons in the Pacific Ocean and Maritime
506 Continent.

507
508 SAI is a far more feasible method of SRM than SD (Shepherd, 2009), but it produces
509 far larger differences in various climate fields from GHG and historic simulations than
510 does SD (Vioni et al., 2021), and far larger across-ESM differences as the models
511 process the aerosol impacts in varied ways (Vioni et al., 2021). The differences in



512 winds noted in G6sulfur likely arise from differences in stratospheric heating due to the
513 sulfur aerosols that then drive tropospheric circulation changes (Visioni et al., 2020).

514

515 Although ESM can provide reliable predictions of the ITF transport, the accuracy of
516 global meso- and small-scale spatial and seasonal changes remains an issue. These
517 relatively small-scale differences are potentially more important for local impacts than
518 differences in larger scale or annual changes. These aspects will need to be explored
519 using impact models tailored to the region, ideally through initiatives focused on the
520 Global South like the Degrees Initiative (<https://www.degrees.ngo/>) and addressing
521 concerns raised by local rightsholders.

522

523 **Code and data availability**

524 All model data used in this work are available from the Earth System Grid Federation
525 (WCRP, 2022; <https://esgf-node.llnl.gov/projects/cmip6>, last access: 3 July 2022).

526 **Author contributions**

527 JCM conceived and designed the analysis. CS collected the data and performed the
528 analysis. CS and JCM wrote the paper. All authors contributed to the discussion.

529 **Competing interests**

530 The contact author has declared that neither they nor their co-authors have any
531 competing interests.

532 **Financial support**

533 This research has been supported by the National Key Research and Development
534 Program of China (grant nos. 2021YFB3900105), State Key Laboratory of Earth
535 Surface Processes and Resource Ecology (2022-ZD-05) and Finnish Academy
536 COLD Consortium (grant no. 322430).

537

538 **References**

539 Alory, G., Wijffels, S., and Meyers, G.: Observed temperature trends in the Indian Ocean over 1960–
540 1999 and associated mechanisms, *Geophys. Res. Lett.*, 34,
541 <https://doi.org/10.1029/2006gl028044>, 2007.



- 542 Amante, C., and Eakins, B. W.: ETOPO1 arc-minute global relief model: procedures, data sources and
543 analysis, NOAA Tech. Memo. NESDIS NGDC-24, <https://doi.org/10.7289/V5C8276M>, 2009.
- 544 Andersson, H. C., and Stigebrandt, A.: Regulation of the Indonesian throughflow by baroclinic draining
545 of the North Australian Basin, *Deep Sea Res., Part I*, 52, 2214-2233,
546 <https://doi.org/10.1016/j.dsr.2005.06.014>, 2005.
- 547 Ayers, J. M., Strutton, P. G., Coles, V. J., Hood, R. R., and Matear, R. J.: Indonesian throughflow nutrient
548 fluxes and their potential impact on Indian Ocean productivity, *Geophys. Res. Lett.*, 41, 5060-
549 5067, <https://doi.org/10.1002/2014gl060593>, 2014.
- 550 Boucher, O., Servonnat, J., Albright, A. L., Aumont, O., Balkanski, Y., Bastrikov, V., Bekki, S., Bonnet,
551 R., Bony, S., Bopp, L., Braconnot, P., Brockmann, P., Cadule, P., Caubel, A., Cheruy, F., Codron,
552 F., Cozic, A., Cugnet, D., D'Andrea, F., Davini, P., Lavergne, C., Denvil, S., Deshayes, J.,
553 Devilliers, M., Ducharne, A., Dufresne, J. L., Dupont, E., Éthé, C., Fairhead, L., Falletti, L.,
554 Flavoni, S., Foujols, M. A., Gardoll, S., Gastineau, G., Ghattas, J., Grandpeix, J. Y., Guenet, B.,
555 Guez, L. E., Guilyardi, E., Guimberteau, M., Hauglustaine, D., Hourdin, F., Idelkadi, A.,
556 Joussaume, S., Kageyama, M., Khodri, M., Krinner, G., Lebas, N., Levvasseur, G., Lévy, C.,
557 Li, L., Lott, F., Lurton, T., Luysaert, S., Madec, G., Madeleine, J. B., Maignan, F., Marchand,
558 M., Marti, O., Mellul, L., Meurdesoif, Y., Mignot, J., Musat, I., Ottlé, C., Peylin, P., Planton, Y.,
559 Polcher, J., Rio, C., Rochetin, N., Rousset, C., Sepulchre, P., Sima, A., Swingedouw, D., Thié
560 blement, R., Traore, A. K., Vancoppenolle, M., Vial, J., Vialard, J., Viovy, N., and Vuichard, N.:
561 Presentation and Evaluation of the IPSL -CM6A-LR Climate Model, *J. Adv. Model. Earth Syst.*,
562 12, <https://doi.org/10.1029/2019ms002010>, 2020.
- 563 Clarke, A. J., and Liu, X.: Interannual sea level in the northern and eastern Indian Ocean, *J. Phys.*
564 *Oceanogr.*, 24, 1224-1235, [https://doi.org/10.1175/1520-
565 0485\(1994\)024<1224:ISLITN>2.0.CO;2](https://doi.org/10.1175/1520-0485(1994)024<1224:ISLITN>2.0.CO;2), 1994.
- 566 Danabasoglu, G., Lamarque, J. F., Bacmeister, J., Bailey, D. A., DuVivier, A. K., Edwards, J., Emmons,
567 L. K., Fasullo, J., Garcia, R., Gettelman, A., Hannay, C., Holland, M. M., Large, W. G.,
568 Lauritzen, P. H., Lawrence, D. M., Lenaerts, J. T. M., Lindsay, K., Lipscomb, W. H., Mills, M.
569 J., Neale, R., Oleson, K. W., Otto-Bliesner, B., Phillips, A. S., Sacks, W., Tilmes, S.,
570 Kampenhout, L., Vertenstein, M., Bertini, A., Dennis, J., Deser, C., Fischer, C., Fox-Kemper,
571 B., Kay, J. E., Kinnison, D., Kushner, P. J., Larson, V. E., Long, M. C., Mickelson, S., Moore,
572 J. K., Nienhouse, E., Polvani, L., Rasch, P. J., and Strand, W. G.: The Community Earth System
573 Model Version 2 (CESM2), *J. Adv. Model. Earth Syst.*, 12,
574 <https://doi.org/10.1029/2019ms001916>, 2020.
- 575 Duan, J., Chen, Z., and Wu, L.: Projected changes of the low-latitude north-western Pacific wind-driven
576 circulation under global warming, *Geophys. Res. Lett.*, 44, 4976-4984,
577 <https://doi.org/10.1002/2017gl073355>, 2017.
- 578 Dubois, M., Rossi, V., Ser-Giacomi, E., Arnaud-Haond, S., López, C., and Hernández-García, E.: Linking
579 basin-scale connectivity, oceanography and population dynamics for the conservation and
580 management of marine ecosystems, *Global Ecol. Biogeogr.*, 25, 503-515,
581 <https://doi.org/10.1111/geb.12431>, 2016.
- 582 Durgadoo, J. V., Rühls, S., Biastoch, A., and Böning, C. W. B.: Indian Ocean sources of Agulhas leakage,
583 *J. Geophys. Res.: Oceans*, 122, 3481-3499, <https://doi.org/10.1002/2016jc012676>, 2017.
- 584 England, M. H., and Huang, F.: On the interannual variability of the Indonesian Throughflow and its
585 linkage with ENSO, *J. Clim.*, 18, 1435-1444, <https://doi.org/10.1175/JCLI3322.1>, 2005.



- 586 Eyring, V., Bony, S., Meehl, G. A., Senior, C. A., Stevens, B., Stouffer, R. J., and Taylor, K. E.: Overview
587 of the Coupled Model Intercomparison Project Phase 6 (CMIP6) experimental design and
588 organization, *Geosci. Model Dev.*, 9, 1937-1958, <https://doi.org/10.5194/gmd-9-1937-2016>,
589 2016.
- 590 Feng, M., Böning, C., Biastoch, A., Behrens, E., Weller, E., and Masumoto, Y.: The reversal of the multi-
591 decadal trends of the equatorial Pacific easterly winds, and the Indonesian Throughflow and
592 Leeuwin Current transports, *Geophys. Res. Lett.*, 38, L11604,
593 <https://doi.org/10.1029/2011gl047291>, 2011.
- 594 Feng, M., Sun, C., Matear, R. J., Chamberlain, M. A., Craig, P., Ridgway, K. R., and Schiller, A.: Marine
595 Downscaling of a Future Climate Scenario for Australian Boundary Currents, *J. Clim.*, 25, 2947-
596 2962, <https://doi.org/10.1175/jcli-d-11-00159.1>, 2012.
- 597 Feng, M., Wijffels, S., Godfrey, S., and Meyers, G.: Do eddies play a role in the momentum balance of
598 the Leeuwin Current?, *J. Phys. Oceanogr.*, 35, 964-975, <https://doi.org/10.1175/JPO2730.1>,
599 2005.
- 600 Feng, M., Zhang, X., Sloyan, B., and Chamberlain, M.: Contribution of the deep ocean to the centennial
601 changes of the Indonesian Throughflow, *Geophys. Res. Lett.*, 44, 2859-2867,
602 <https://doi.org/10.1002/2017gl072577>, 2017.
- 603 Gertler, C. G., O'Gorman, P. A., Kravitz, B., Moore, J. C., Phipps, S. J., and Watanabe, S.: Weakening of
604 the Extratropical Storm Tracks in Solar Geoengineering Scenarios, *Geophys. Res. Lett.*, 47,
605 <https://doi.org/10.1029/2020gl087348>, 2020.
- 606 Gill, A. E., and Adrian, E.: *Atmosphere-ocean dynamics: Academic press*, 30 pp., ISBN0122835220,
607 1982.
- 608 Godfrey, J., Wilkin, J., and Hirst, A.: Why does the Indonesian Throughflow appear to originate from the
609 North Pacific?, *J. Phys. Oceanogr.*, 23, 1087-1098, [https://doi.org/10.1175/1520-
610 0485\(1993\)023%3C1087:WDTITA%3E2.0.CO;2](https://doi.org/10.1175/1520-0485(1993)023%3C1087:WDTITA%3E2.0.CO;2), 1993.
- 611 Godfrey, J. S.: A sverdrup model of the depth-integrated flow for the world ocean allowing for island
612 circulations, *Geophys. Astrophys. Fluid Dyn.*, 45, 89-112,
613 <https://doi.org/10.1080/03091928908208894>, 1989.
- 614 Godfrey, J. S.: The effect of the Indonesian throughflow on ocean circulation and heat exchange with the
615 atmosphere: A review, *J. Geophys. Res.: Oceans*, 101, 12217-12237,
616 <https://doi.org/10.1029/95jc03860>, 1996.
- 617 Gordon, A. L.: Inter-ocean exchange of thermocline water, *J. Geophys. Res.: Oceans*, 91, 5037-5046,
618 <https://doi.org/10.1029/JC091iC04p05037>, 1986.
- 619 Gordon, A. L.: The Indonesian Seas, *Oceanogr.*, 18, 14, <https://doi.org/10.5670/oceanog.2005.01>, 2005.
- 620 Gorgues, T., Menkes, C., Aumont, O., Dandonneau, Y., Madec, G., and Rodgers, K.: Indonesian
621 throughflow control of the eastern equatorial Pacific biogeochemistry, *Geophys. Res. Lett.*, 34,
622 <https://doi.org/10.1029/2006gl028210>, 2007.
- 623 Guo, A., Moore, J. C., and Ji, D.: Tropical atmospheric circulation response to the G1 sunshade
624 geoengineering radiative forcing experiment, *Atmos. Chem. Phys.*, 18, 8689-8706,
625 <https://doi.org/10.5194/acp-18-8689-2018>, 2018.
- 626 Hirst, A. C., and Godfrey, J.: The response to a sudden change in Indonesian throughflow in a global
627 ocean GCM, *J. Phys. Oceanogr.*, 24, 1895-1910, [https://doi.org/10.1175/1520-
628 0485\(1994\)024<1895:TRTASC>2.0.CO;2](https://doi.org/10.1175/1520-0485(1994)024<1895:TRTASC>2.0.CO;2), 1994.
- 629 Hong, Y., Moore, J. C., Jevrejeva, S., Ji, D., Phipps, S. J., Lenton, A., Tilmes, S., Watanabe, S., and Zhao,



- 630 L.: Impact of the GeoMIP G1 sunshade geoengineering experiment on the Atlantic meridional
631 overturning circulation, *Environ. Res. Lett.*, 12, <https://doi.org/10.1088/1748-9326/aa5fb8>,
632 2017.
- 633 Hu, D., Wu, L., Cai, W., Gupta, A. S., Ganachaud, A., Qiu, B., Gordon, A. L., Lin, X., Chen, Z., Hu, S.,
634 Wang, G., Wang, Q., Sprintall, J., Qu, T., Kashino, Y., Wang, F., and Kessler, W. S.: Pacific
635 western boundary currents and their roles in climate, *Nat.*, 522, 299-308,
636 <https://doi.org/10.1038/nature14504>, 2015.
- 637 Hu, S., and Sprintall, J.: Interannual variability of the Indonesian Throughflow: The salinity effect, *J.*
638 *Geophys. Res.: Oceans*, 121, 2596-2615, <https://doi.org/10.1002/2015jc011495>, 2016.
- 639 Kravitz, B., Robock, A., Tilmes, S., Boucher, O., English, J. M., Irvine, P. J., Jones, A., Lawrence, M. G.,
640 MacCracken, M., Muri, H., Moore, J. C., Niemeier, U., Phipps, S. J., Sillmann, J., Storelvmo,
641 T., Wang, H., and Watanabe, S.: The Geoengineering Model Intercomparison Project Phase 6
642 (GeoMIP6): simulation design and preliminary results, *Geosci. Model Dev.*, 8, 3379-3392,
643 <https://doi.org/10.5194/gmd-8-3379-2015>, 2015.
- 644 Kriegler, E., O'Neill, B. C., Hallegatte, S., Kram, T., Lempert, R. J., Moss, R. H., and Wilbanks, T.: The
645 need for and use of socio-economic scenarios for climate change analysis: A new approach
646 based on shared socio-economic pathways, *Global Environ. Change*, 22, 807-822,
647 <https://doi.org/10.1016/j.gloenvcha.2012.05.005>, 2012.
- 648 Lee, T., Fukumori, I., Menemenlis, D., Xing, Z., and Fu, L.-L.: Effects of the Indonesian throughflow on
649 the Pacific and Indian Oceans, *J. Phys. Oceanogr.*, 32, 1404-1429, [https://doi.org/10.1175/1520-0485\(2002\)032<1404:EOTITO>2.0.CO;2](https://doi.org/10.1175/1520-0485(2002)032<1404:EOTITO>2.0.CO;2), 2002.
- 651 Lukas, R., Yamagata, T., and McCreary, J. P.: Pacific low-latitude western boundary currents and the
652 Indonesian throughflow, *J. Geophys. Res.: Oceans*, 101, 12209-12216,
653 <https://doi.org/10.1029/96jc01204>, 1996.
- 654 MacMartin, D. G., and Kravitz, B.: Dynamic climate emulators for solar geoengineering, *Atmos. Chem.*
655 *Phys.*, 16, 15789-15799, <https://doi.org/10.5194/acp-16-15789-2016>, 2016.
- 656 Mauritsen, T., Bader, J., Becker, T., Behrens, J., Bittner, M., Brokopf, R., Brovkin, V., Claussen, M.,
657 Crueger, T., Esch, M., Fast, I., Fiedler, S., Flaschner, D., Gayler, V., Giorgetta, M., Goll, D. S.,
658 Haak, H., Hagemann, S., Hedemann, C., Hohenegger, C., Ilyina, T., Jahns, T., Jimenez-de-la-
659 Cuesta, D., Jungelaus, J., Kleinen, T., Kloster, S., Kracher, D., Kinne, S., Kleberg, D., Lasslop,
660 G., Kornbluh, L., Marotzke, J., Matei, D., Meraner, K., Mikolajewicz, U., Modali, K., Mobis,
661 B., Muller, W. A., Nabel, J., Nam, C. C. W., Notz, D., Nyawira, S. S., Paulsen, H., Peters, K.,
662 Pincus, R., Pohlmann, H., Pongratz, J., Popp, M., Raddatz, T. J., Rast, S., Redler, R., Reick, C.
663 H., Rohrschneider, T., Schemann, V., Schmidt, H., Schnur, R., Schulzweida, U., Six, K. D., Stein,
664 L., Stemmler, I., Stevens, B., von Storch, J. S., Tian, F., Voigt, A., Vrese, P., Wieners, K. H.,
665 Wilkenskjaeld, S., Winkler, A., and Roeckner, E.: Developments in the MPI-M Earth System
666 Model version 1.2 (MPI-ESM1.2) and Its Response to Increasing CO₂, *J. Adv. Model. Earth*
667 *Syst.*, 11, 998-1038, <https://doi.org/10.1029/2018MS001400>, 2019.
- 668 Meyers, G.: Variation of Indonesian throughflow and the El Niño-southern oscillation, *J. Geophys. Res.:*
669 *Oceans*, 101, 12255-12263, <https://doi.org/10.1029/95JC03729>, 1996.
- 670 Moore, J. C., Yue, C., Zhao, L., Guo, X., Watanabe, S., and Ji, D.: Greenland Ice Sheet Response to
671 Stratospheric Aerosol Injection Geoengineering, *Earth. Fut.*, 7, 1451-1463,
672 <https://doi.org/10.1029/2019EF001393>, 2019.
- 673 Muri, H., Tjiputra, J., Otterå, O. H., Adakudlu, M., Lauvset, S. K., Grini, A., Schulz, M., Niemeier, U.,



- 674 and Kristjánsson, J. E.: Climate Response to Aerosol Geoengineering: A Multimethod
675 Comparison, *J. Clim.*, 31, 6319-6340, <https://doi.org/10.1175/jcli-d-17-0620.1>, 2018.
- 676 O'Neill, B. C., Tebaldi, C., Vuuren, D. P. v., Eyring, V., Friedlingstein, P., Hurtt, G., Knutti, R., Kriegler,
677 E., Lamarque, J.-F., and Lowe, J.: The scenario model intercomparison project (ScenarioMIP)
678 for CMIP6, *Geosci. Model Dev.*, 9, 3461-3482, <https://doi.org/10.5194/gmd-9-3461-2016>, 2016.
- 679 Potemra, J. T., Lukas, R., and Mitchum, G. T.: Large-scale estimation of transport from the Pacific to the
680 Indian Ocean, *J. Geophys. Res.: Oceans*, 102, 27795-27812, <https://doi.org/10.1029/97jc01719>,
681 1997.
- 682 Rezaei, A., Karami, K., Tilmes, S., and Moore, J. C.: Changes in global teleconnection patterns under
683 global warming and stratospheric aerosol intervention scenarios, *EGUsphere* [preprint], 1-25,
684 <https://doi.org/10.5194/egusphere-2022-974>, 2022.
- 685 Séférian, R., Nabat, P., Michou, M., Saint-Martin, D., Voldoire, A., Colin, J., Decharme, B., Delire, C.,
686 Berthet, S., Chevallier, M., Sénési, S., Franchisteguy, L., Vial, J., Mallet, M., Joetzjer, E.,
687 Geoffroy, O., Guérémy, J. F., Moine, M. P., Msadek, R., Ribes, A., Rocher, M., Roehrig, R.,
688 Salas-y-Méllia, D., Sanchez, E., Terray, L., Valcke, S., Waldman, R., Aumont, O., Bopp, L.,
689 Deshayes, J., Éthé, C., and Madec, G.: Evaluation of CNRM Earth System Model, CNRM-
690 ESM2-1: Role of Earth System Processes in Present-Day and Future Climate, *J. Adv. Model.*
691 *Earth Syst.*, 11, 4182-4227, <https://doi.org/10.1029/2019ms001791>, 2019.
- 692 Sellar, A. A., Jones, C. G., Mulcahy, J. P., Tang, Y., Yool, A., Wiltshire, A., O'Connor, F. M., Stringer, M.,
693 Hill, R., Palmieri, J., Woodward, S., Mora, L., Kuhlbrodt, T., Rumbold, S. T., Kelley, D. I., Ellis,
694 R., Johnson, C. E., Walton, J., Abraham, N. L., Andrews, M. B., Andrews, T., Archibald, A. T.,
695 Berthou, S., Burke, E., Blockley, E., Carslaw, K., Dalvi, M., Edwards, J., Folberth, G. A.,
696 Gedney, N., Griffiths, P. T., Harper, A. B., Hendry, M. A., Hewitt, A. J., Johnson, B., Jones, A.,
697 Jones, C. D., Keeble, J., Liddicoat, S., Morgenstern, O., Parker, R. J., Predoi, V., Robertson, E.,
698 Siahann, A., Smith, R. S., Swaminathan, R., Woodhouse, M. T., Zeng, G., and Zerroukat, M.:
699 UKESM1: Description and Evaluation of the U.K. Earth System Model, *J. Adv. Model. Earth*
700 *Syst.*, 11, 4513-4558, <https://doi.org/10.1029/2019ms001739>, 2019.
- 701 Sen Gupta, A., Ganachaud, A., McGregor, S., Brown, J. N., and Muir, L.: Drivers of the projected
702 changes to the Pacific Ocean equatorial circulation, *Geophys. Res. Lett.*, 39, L09605,
703 <https://doi.org/10.1029/2012gl051447>, 2012.
- 704 Sen Gupta, A., McGregor, S., Seville, E., Ganachaud, A., Brown, J. N., and Santoso, A.: Future changes
705 to the Indonesian Throughflow and Pacific circulation: The differing role of wind and deep
706 circulation changes, *Geophys. Res. Lett.*, 43, 1669-1678, <https://doi.org/10.1002/2016gl067757>,
707 2016.
- 708 Sen Gupta, A., Stellema, A., Pontes, G. M., Taschetto, A. S., Verges, A., and Rossi, V.: Future changes to
709 the upper ocean Western Boundary Currents across two generations of climate models, *Sci. Rep.*,
710 11, 9538, <https://doi.org/10.1038/s41598-021-88934-w>, 2021.
- 711 Shepherd, J. G.: *Geoengineering the climate: science, governance and uncertainty*: Royal Society,
712 London, 98 pp., ISBN085403773X, 2009.
- 713 Shinoda, T., Han, W., Metzger, E. J., and Hurlburt, H. E.: Seasonal Variation of the Indonesian
714 Throughflow in Makassar Strait, *J. Phys. Oceanogr.*, 42, 1099-1123,
715 <https://doi.org/10.1175/jpo-d-11-0120.1>, 2012.
- 716 Smyth, J. E., Russotto, R. D., and Storelvmo, T.: Thermodynamic and dynamic responses of the
717 hydrological cycle to solar dimming, *Atmos. Chem. Phys.*, 17, 6439-6453,



- 718 <https://doi.org/10.5194/acp-17-6439-2017>, 2017.
- 719 Sprintall, J., Wijffels, S. E., Molcard, R., and Jaya, I.: Direct estimates of the Indonesian Throughflow
720 entering the Indian Ocean: 2004–2006, *J. Geophys. Res.*, 114,
721 <https://doi.org/10.1029/2008jc005257>, 2009.
- 722 Stigebrandt, A.: The North Pacific: A global-scale estuary, *J. Phys. Oceanogr.*, 14, 464-470,
723 [https://doi.org/10.1175/1520-0485\(1984\)014<0464:TNPAGS>2.0.CO;2](https://doi.org/10.1175/1520-0485(1984)014<0464:TNPAGS>2.0.CO;2), 1984.
- 724 Susanto, R. D., and Song, Y. T.: Indonesian throughflow proxy from satellite altimeters and gravimeters,
725 *J. Geophys. Res.: Oceans*, 120, 2844-2855, <https://doi.org/10.1002/2014jc010382>, 2015.
- 726 Sverdrup, H. U.: Wind-driven currents in a baroclinic ocean; with application to the equatorial currents
727 of the eastern Pacific, *Proc. Natl. Acad. Sci. U. S. A.*, 33, 318,
728 <https://doi.org/10.1073/pnas.33.11.318>, 1947.
- 729 Talley, L. D.: Freshwater transport estimates and the global overturning circulation: Shallow, deep and
730 throughflow components, *Prog. Oceanogr.*, 78, 257-303,
731 <https://doi.org/10.1016/j.pocean.2008.05.001>, 2008.
- 732 Tilmes, S., MacMartin, D. G., Lenaerts, J. T. M., van Kampenhout, L., Muntjewerf, L., Xia, L., Harrison,
733 C. S., Krumhardt, K. M., Mills, M. J., Kravitz, B., and Robock, A.: Reaching 1.5 and 2.0 °C
734 global surface temperature targets using stratospheric aerosol geoengineering, *Earth Syst.*
735 *Dynam.*, 11, 579-601, <https://doi.org/10.5194/esd-11-579-2020>, 2020.
- 736 van Vuuren, D. P., Edmonds, J., Kainuma, M., Riahi, K., Thomson, A., Hibbard, K., Hurtt, G. C., Kram,
737 T., Krey, V., Lamarque, J.-F., Masui, T., Meinshausen, M., Nakicenovic, N., Smith, S. J., and
738 Rose, S. K.: The representative concentration pathways: an overview, *Clim. Change*, 109, 5-31,
739 <https://doi.org/10.1007/s10584-011-0148-z>, 2011.
- 740 Vecchi, G. A., and Soden, B. J.: Global Warming and the Weakening of the Tropical Circulation, *J. Clim.*,
741 20, 4316-4340, <https://doi.org/10.1175/jcli4258.1>, 2007.
- 742 Vincent, D. G.: The South Pacific convergence zone (SPCZ): A review, *Mon. Weather Rev.*, 122, 1949-
743 1970, [https://doi.org/10.1175/1520-0493\(1994\)122<1949:TSPCZA>2.0.CO;2](https://doi.org/10.1175/1520-0493(1994)122<1949:TSPCZA>2.0.CO;2), 1994.
- 744 Visioni, D., MacMartin, D. G., Kravitz, B., Boucher, O., Jones, A., Lurton, T., Martine, M., Mills, M. J.,
745 Nabat, P., Niemeier, U., Séférian, R., and Tilmes, S.: Identifying the sources of uncertainty in
746 climate model simulations of solar radiation modification with the G6sulfur and G6solar
747 Geoengineering Model Intercomparison Project (GeoMIP) simulations, *Atmos. Chem. Phys.*,
748 21, 10039-10063, <https://doi.org/10.5194/acp-21-10039-2021>, 2021.
- 749 Visioni, D., MacMartin, D. G., Kravitz, B., Lee, W., Simpson, I. R., and Richter, J. H.: Reduced Poleward
750 Transport Due to Stratospheric Heating Under Stratospheric Aerosols Geoengineering, *Geophys.*
751 *Res. Lett.*, 47, <https://doi.org/10.1029/2020gl089470>, 2020.
- 752 Wajsowicz, R. C.: The circulation of the depth-integrated flow around an island with application to the
753 Indonesian Throughflow, *J. Phys. Oceanogr.*, 23, 1470-1484, [https://doi.org/10.1175/1520-0485\(1993\)023<1470:TCOTDI>2.0.CO;2](https://doi.org/10.1175/1520-0485(1993)023<1470:TCOTDI>2.0.CO;2), 1993.
- 754 Wang, Q., Moore, J. C., and Ji, D.: A statistical examination of the effects of stratospheric sulfate
755 geoengineering on tropical storm genesis, *Atmos. Chem. Phys.*, 18, 9173-9188,
756 <https://doi.org/10.5194/acp-18-9173-2018>, 2018.
- 757 Wyrtki, K.: Indonesian through flow and the associated pressure gradient, *J. Geophys. Res.: Oceans*, 92,
758 12941-12946, <https://doi.org/10.1029/JC092iC12p12941>, 1987.
- 759 Xie, M., Moore, J. C., Zhao, L., Wolovick, M., and Muri, H.: Impacts of three types of solar
760 geoengineering on the Atlantic Meridional Overturning Circulation, *Atmos. Chem. Phys.*, 22,
761

<https://doi.org/10.5194/esd-2023-6>
Preprint. Discussion started: 7 March 2023
© Author(s) 2023. CC BY 4.0 License.



762 4581-4597, <https://doi.org/10.5194/acp-22-4581-2022>, 2022.
763